Electrochimica Acta 565 (2026) 148753

Contents lists available at ScienceDirect

Electrochimica Acta

journal homepage: www.journals.elsevier.com/electrochimica-acta

Development of a predictive model for performance analysis of anion exchange membrane electrolysers

Riccardo Venturino [a], Alessio D'Alessandro [b], Laura Traversone [b], Fiammetta Rita Bianchi [a,*], Barbara Bosio [a]

[a] Department of Civil, Chemical and Environmental Engineering (DICCA), University of Genoa, Via Opera Pia 15, 16145 Genova, Italy
[b] Ansaldo Green Tech, via Nicola Lorenzi 8, 16152 Genova, Italy

ARTICLE INFO

Keywords:
Water electrolysis
Anion exchange membrane
Electrochemical kinetics
Bubble effects
Cell performance modelling

ABSTRACT

Anion Exchange Membrane (AEM) water electrolysis is a promising solution for hydrogen production that consists of low-cost metals as the electrocatalyst and low-concentration alkaline solutions as the electrolyte, overcoming common issues of other low-temperature cells. This technology is investigated by developing an in-home-built Python model able to predict AEM electrolyser electrochemical performance under a dry cathode configuration as a function of applied working conditions and microstructural parameters. Polarisation losses derive from electrochemistry principles and consider effects due to the presence of bubbles that form on the electrode surface and evolve within the electrolyte. It is noteworthy that the asymmetric behaviour of AEM cells requires specific assumptions and equations for each side in view of different anodic and cathodic environments. Following the model is preliminarily validated through an ad hoc testing campaign on a lab-scale cell. Simulation results allow for identifying the limiting factors (i.e., current and solution molarity), distinguishing different polarisation losses (activation and ohmic loss as the predominant factor in high and low concentrated alkaline solutions, respectively), and quantifying losses due to bubbles (around 8% of total polarisation in the worst case). In detail, the bubbles generate turbulence within the liquid, favouring the reactant diffusion mechanisms, but decrease the effective active area and the electrolyte conductivity, resulting in the predominant effect.

1. Introduction

The extensive use of fossil fuels in the current energy infrastructure is the main source of anthropogenic carbon dioxide emissions, which significantly contribute to global warming and climate change. The decline in crude oil reserves and some stricter emission regulations are driving the search for alternative fuels and energy vectors. They should be economically competitive, environmentally sustainable, easily available, and practical and reliable to use. Hydrogen is one of the most promising solutions, showing a higher specific energy content than conventional fuels (120 MJ/kg H_2 vs. 50 MJ/kg CH_4 vs. 44 MJ/kg gasoline (LHV)). Nevertheless, it is primarily found in the form of compounds with other elements, making molecular hydrogen production quite challenging. Hydrogen is derived mainly from the conversion of natural gas and other light hydrocarbons through steam reforming and partial oxidation, resulting in significant greenhouse gas emissions. Water electrolysis is a promising solution among several understudied processes, including biomass thermochemical conversion, photochemical and photocatalytic conversion [1]. Indeed, coupling with renewables and obtaining oxygen as a byproduct allow for green hydrogen synthesis with minimum environmental impacts [3].

Nevertheless, electrolysers still have several issues correlated to material costs, electricity consumption, and long-term cell operation in view of mechanical and chemical instability, making them little competitive on the energy market [2–4]. Merging the main benefits of low-temperature cells, Anion Exchange Membrane Electrolysis Cells (AEMECs) are a promising solution. This technology derives from alkaline water electrolysis, where the conventional diaphragms are replaced with an anion exchange membrane (i.e., quaternary ammonium ion exchange membranes). Moreover, a low-concentration alkaline solution can be used as the electrolyte, different from alkaline electrolysers (1 vs. 5 M KOH). Anodic and cathodic electrode materials are transition metal-based electrocatalysts, particularly nickel alloy and Ni-Fe-Co materials, which are cheaper than noble metal catalysts used in proton exchange membrane electrolysers [5,6].

AEM electrolysis consists of splitting water molecules into hydrogen and oxygen through two half-reactions: water reduction at the cathode

* Corresponding author.
E-mail address: fiammettarita.bianchi@unige.it (F.R. Bianchi).

https://doi.org/10.1016/j.electacta.2026.148753
Received 24 December 2025; Received in revised form 25 March 2026; Accepted 25 March 2026
Available online 27 March 2026

Nomenclature

A, A_{eff}	Geometrical and effective active area
A_{bubble}, $\overline{A}_{bubble}$	Area and average area of a single bubble
$\tilde{a}$, $\tilde{b}$	Empirical parameters to compute water saturation pressure in KOH alkaline solution
a	Activity
b	Kinetic constant for bubble growth
C	Concentration
C^{bulk}, C^{memb}, C^{sur}	Bulk, electrode-membrane interface, electrode surface concentrations
C^{AEM}	Ion concentration within membrane
D, D^{eff}	Molecular diffusion and effective diffusion coefficients
d_{an}, d_{cat}, d_{memb}	Anodic catalyst layer, cathodic catalyst layer, membrane thicknesses
E_{act}	Activation energy
ΔE_{cell}	Cell voltage
ΔE_{rev}, ΔE^0_{rev}	Reversible voltage and reversible voltage at reference status
F	Faraday constant
f_{gas}	Gas flow rate
H	Henry's constant
IEC	Ion Exchange Capacity of membrane
j	Current density
j_o	Exchange current density
J	Current for the unit of volume
J_{av}	Average current for the unit of volume
K_D	Donnan equilibrium constant
k, $\tilde{k}$, $\tilde{k}^*$	Kinetic constants
k_{diff}	Corrective term of diffusion coefficient due to bubble presence
M	Molarity
m	Molality
MM	Molecular weight
$N_{bubbles}$	Number of bubbles
p	Pressure
p_{ref}	Reference pressure (i.e., atmospheric value)
$p^{sat}_{H_2O}$, p^{sat}_{KOH}	Pure water and KOH alkaline solution saturation pressures
R	Ideal gas constant
r, r_{max}	Bubble radius and its maximum value before detachment
T	Temperature
t_r	Bubble residence time
u	Ion mobility
V	Dimensionless diffusion volume
x	Spatial coordinate in material balances
z	Charge number

Greek letters

α	Charge transfer coefficient
β, γ, β^*, γ^*	Kinetic orders
δ_{an}, δ_{cat}	Anodic and cathodic gas diffusion layer thicknesses
ε	Phase volume fraction
η	Polarisation loss
η_{act}, η_{diff}, η_{ohm}	Activation, diffusion, ohmic overpotentials
ϑ	Coverage factor due to bubbles
λ	Ion transport number
ρ_{an}, ρ_{cat}, ρ_{memb}, ρ_{ohm}, ρ_{pol}	Anode, cathode and membrane specific resistances, ohmic and polarization resistances from EIS
σ_{KOH}, σ_{ion}, σ_{memb}	KOH solution, ionomer, membrane conductivities
τ	Electrode tortuosity
ϕ	Current density fraction generating dissolved oxygen
φ	Bubble contact angle

generates hydroxide ions that migrate to the anode, where the oxygen evolution releases water (Eq. (1), Eq. (2), Eq. (3)). According to the operation, alkaline solution can be fed to both sides of the cell or just at the anode, exploiting its permeation across the membrane to provide the needed water for the hydrogen cathodic evolution [7]. Working below 100 °C, hydrogen and oxygen production results in bubble formation and evolution with significant impacts on the cell performance [8]. Indeed, the bubble formation on the electrode reduces the available surface, partially covering the reaction sites. Moreover, their motion within the electrolyte influences both the charge migration by reducing the alkaline solution conductivity and the material transport by generating some turbulence within the system.

$$\text{Cathode}: \quad 2H_2O + 2e^- \rightarrow H_2 + 2OH^-_{(aq)} \tag{1}$$

$$\text{Anode}: \quad 2OH^-_{(aq)} \rightarrow H_2O + \frac{1}{2}O_2 + 2e^- \tag{2}$$

$$\text{Overall reaction}: \quad H_2O \rightarrow H_2 + \frac{1}{2}O_2 \tag{3}$$

In view of the system complexity, multidimensional models have been developed to consider the co-presence of liquid and vapour phases, setting the bases for cell process simulation as well. Commonly, one-direction models have been reported to evaluate the species flux evolution on the cell plane or along the thickness of electrodes and membrane, focusing above all on water exchange between two sides of the membrane [9–14]. CFD-based software has also permitted reaching a higher detail level of pressure and temperature effects on the cell behaviour [7,15–17]. Research facing AEMEC simulation has taken reference to the models previously developed for other low-temperature electrolysers, trying to adjust the differences (i.e., membranes instead of separators, alkaline solutions instead of distilled water and so on). Nevertheless, few works have proposed specific electrochemical formulations for AEM cells, considering the bubble effect on polarisation losses as well as the specific reaction environment at each cell side [18–21].

This paper presents a performance predictive model for AEMEC under dry cathode operation, meaning that no liquid electrolyte is fed to the cathodic compartment, but water fed and produced at the anode migrates across the permeable membrane and reacts at the cathode. Here the cathodic side is characterised by only hydrogen and steam, while the anode consists of an alkaline solution with O_2 evolving bubbles. Firstly, overviewing previous reference works on low-temperature cells, the physically based theoretical formulation was presented by underlining peculiarities of the anion exchange membrane technology operation. Schematising the cell as an electrical circuit, polarisation losses were expressed as a function of easily measurable working conditions, clearly distinguishing the weight of ohmic, activation and diffusion loss among electrodes, electrolyte and membrane. Moreover, the research work evaluated effects due to the bubbles on anodic reaction, oxygen material transport and ion migration, quantifying a bubble overpotential sum of all these phenomena. A preliminary experimental validation checked model assumptions, and finally a sensitivity analysis provided a first investigation of the main cell dependencies at variable current densities, temperatures and fed electrolyte molarities.

2. Methods

2.1. Theoretical formulation

The electrochemical behaviour can be described through I-V curves, following electrochemistry principles and including possible effects due to the bubble anodic evolution. A pseudo 0D steady state system is considered where all physicochemical features derive from a macroscopic perspective, assuming an isothermal cell with negligible pressure drops and homogeneous reactant compositions on its plane. The AEM cell performance is schematised as an electrical circuit to consider occurring polarization losses (Fig. 1). The attended output consists of evaluating the electrolysis cell voltage (ΔE_{cell}) as a function of multiple contributions related to the system thermodynamics, the electrochemical reaction kinetics, the charge migration and the reactant material transport (Eq. (4)).

$$\Delta E_{cell} = \Delta E_{rev} + \eta_{act} + \eta_{ohm} + \eta_{diff} \tag{4}$$

Where ΔE_{rev} represents the reversible voltage and η the overpotentials by distinguishing the anodic and cathodic sides. Polarization losses are computed in terms of homogeneous physicochemical properties, except for the concentration gradients (i.e., diffusion overpotential sources) that derive from simplified material balances along the electrode thickness divided in the Gas Diffusion Layer (GDL) and the Catalyst Layer (CL).

The developed model in the Python script is presented in the following, formulating the equilibrium voltage, the activation and diffusion loss, the ohmic loss and, finally, identifying the bubble effect in terms of a further cell overpotential.

2.1.1. Equilibrium voltage

The minimum required voltage, known as the reversible potential (ΔE_{rev}), is a function of the operating temperature and the reactant compositions according to the Nernst equation (Eq. (5)) [7].

$$\Delta E_{rev} = \Delta E^0_{rev} + \frac{RT}{zF}\ln\left(\frac{a_{H_2}\, a_{O_2}^{1/2}}{a_{H_2O}}\right) \tag{5}$$

$$\Delta E^0_{rev} = 1.229 - 0.9\cdot10^{-3}(T - 298) \tag{6}$$

Where R is the ideal gas constant, T the temperature, z the charge number, F the Faraday constant, a the component activities dependent on their partial pressures at atmospheric conditions (i.e., ideal gas behaviour), ΔE^0_{rev} the reversible voltage at reference status computed through Eq. (6) as a function of the temperature (T in [K]). The water activity calculation assumes the gas/liquid equilibrium achievement (Eq. (7)), deriving from the saturation pressure of pure water ($p^{sat}_{H_2O}$ in [Pa]) dependent on temperature (T in [K]) (Eq. (8)) and correcting it to consider the presence of a KOH aqueous solution (p^{sat}_{KOH} and $p^{sat}_{H_2O}$ in [atm]) (Eq. (9)) [22–23].

$$a_{H_2O} = \frac{p^{sat}_{KOH}}{p^{sat}_{H_2O}} \tag{7}$$

$$p^{sat}_{H_2O} = \exp\left(23.2 - \frac{3816.4}{T - 46.16}\right) \tag{8}$$

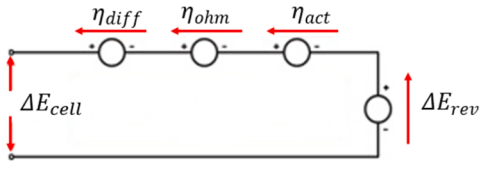

Fig. 1. Electric circuit model for AEM electrolyser.

$$p^{sat}_{KOH} = 10^{\tilde{a}}\left(p^{sat}_{H_2O}\right)^{\tilde{b}} \tag{9}$$

Where the parameters $\tilde{a}$ and $\tilde{b}$ are calculated as a function of the molality (m in [mol/$kg_{solvent}$]) of the KOH aqueous solution (Eq. (10), Eq. (11)) [22].

$$\tilde{a} = -0.01508m - \left(1.6788\cdot10^{-3}\right)m^2 + \left(2.25887\cdot10^{-5}\right)m^3 \tag{10}$$

$$\tilde{b} = 1 - \left(1.2062\cdot10^{-3}\right)m + \left(5.6024\cdot10^{-4}\right)m^2 - \left(7.8228\cdot10^{-6}\right)m^3 \tag{11}$$

It is noteworthy that equal water activity can be assumed at both electrodes due to the high anion conductivity of the membrane that allows a basic environment at the cathodic interface, also without feeding electrolyte solution in dry cathode cell operation. While the activities of hydrogen and oxygen result in Eq. (12), assuming an isothermal behaviour on two sides [7].

$$a_{H_2} = a_{O_2} = \frac{p - p^{sat}_{H_2O}}{p_{ref}} \tag{12}$$

Where p_{ref} is the reference pressure equal to atmospheric one.

2.1.2. Activation and diffusion overpotentials

The activation overpotential (η_{act}) is the energy required to develop the hydrogen and oxygen evolution reactions, while the diffusion overpotential (η_{diff}) is the energy required to overcome material transport limitations of reactant/produced species, considering their concentration gradients along the electrode thickness. Both terms can be derived as two limiting conditions from the Butler-Volmer equation, which expresses the electrochemical reaction rate in terms of the current density (Eq. (13), Eq. (14), where the oxidation is the direct reaction) [24–25]. Indeed, it depends on the reactant surface concentrations and the temperature, as in the case of a chemical reaction, as well as on the applied polarization ($\eta = \eta_{act} + \eta_{diff}$).

$$j = zF\left\{k_{ox}\exp\left[\frac{\alpha zF\left(\Delta E_{rev} - \Delta E^0_{rev}\right)}{RT}\right]\prod_i\left(C_i^{sur}\right)^{\gamma_i}\exp\left(\frac{\alpha zF\eta}{RT}\right) - k_{red}\exp\left[\frac{-(1-\alpha)zF\left(\Delta E_{rev} - \Delta E^0_{rev}\right)}{RT}\right]\prod_i\left(C_i^{sur}\right)^{\beta_i}\exp\left[\frac{-(1-\alpha)zF\eta}{RT}\right]\right\} \tag{13}$$

$$j = j_o\left\{\prod_i\left(\frac{C_i^{sur}}{C_i^{bulk}}\right)^{\gamma_i}\exp\left(\frac{\alpha zF\eta}{RT}\right) - \prod_i\left(\frac{C_i^{sur}}{C_i^{bulk}}\right)^{\beta_i}\exp\left[\frac{-(1-\alpha)zF\eta}{RT}\right]\right\} \tag{14}$$

Where k are the kinetic constants referring to direct (i.e., oxidation) and indirect (i.e., reduction) reactions, α the charge transfer coefficient, j the current density, j_o the exchange current density, C^{sur} and C^{bulk} the concentrations on the electrode surface and in the bulk, γ and β on the kinetic orders for direct (i.e., oxidation) and indirect (i.e., reduction) reactions, respectively.

The activation overpotential derives from a simplified Butler–Volmer equation if negligible concentration gradients between active sites and bulk are assumed, resulting in Eq. (15) and Eq. (16) (oxidation as the direct reaction) for the cathode and the anode, respectively. It is noteworthy that the bubble evolution reduces the available surface area; here, the bubble coverage fraction (ϑ) is included at the anode [26].

$$j = j_0^{cat}\left\{\exp\left(\frac{\alpha_{cat}\, zF\eta^{cat}_{act}}{RT}\right) - \exp\left[\frac{-(1-\alpha_{cat})zF\eta^{cat}_{act}}{RT}\right]\right\} \tag{15}$$

$$\frac{j}{(1-\vartheta)} = j_0^{an}\left\{\exp\left(\frac{\alpha_{an}zF\eta^{an}_{act}}{RT}\right) - \exp\left[\frac{-(1-\alpha_{an})zF\eta^{an}_{act}}{RT}\right]\right\} \tag{16}$$

The exchange current density is defined as the reaction rate at the equilibrium conditions when the net current density is zero, matching

the direct and indirect process rates. Developing the Butler-Volmer equation and explicating the temperature dependence of the kinetic constants according to an Arrhenius-type law, Eq. (17) and Eq. (18) are obtained, where the exchange current densities are a function of the activation energies (E_{act}), the pre-exponential coefficients considering specific electrode microstructures ($\widetilde{k}$) and the reactant bulk concentrations to the power of partial reaction orders (γ). Refer to the Appendix section for the complete theoretical formulation of exchange current densities.

$$j_0^{cat} = \widetilde{k}_{cat}^{*}\left(C_{-(cat)}^{bulk}\right)^{\gamma_2^{*}} \exp\left(\frac{-E_{act}^{cat}}{RT}\right) \tag{17}$$

$$j_0^{an} = \widetilde{k}_{an}^{*}\left(C_{-(an)}^{bulk}\right)^{\gamma^{*}} \exp\left(\frac{-E_{act}^{an}}{RT}\right) \tag{18}$$

Where C_{-}^{bulk} refers to OH^- concentration in the bulk.

At the anode (Eq. (16)) the oxygen evolution occurs within the liquid electrolyte; bubbles forming on the electrode surface cause a decrease in the effective active area until they detach. This effect is considered by the bubble coverage factor, which allows for calculating the effective active surface dependent on the total number of bubbles and the average area of a single bubble. Following the approach presented in [27] and summarised in the Appendix section, a semi-empirical correlation is applied as a function of current density (j in [A/m^2]) in Eq. (19), as already used in previous literature works on AEM electrolysis cells [20–26].

$$\vartheta = \mathrm{costf}_{gas} \cong 0.023\ j^{0.3} \tag{19}$$

Where f_{gas} is the gas volumetric flowrate.

This formula has been validated for the whole range of the coverage factor in the case of a stagnant electrolyte (i.e., an electrolyte without flow and with unhindered bubble release), considering the oxygen evolution reaction on Ni-based electrocatalysts at around 1 M KOH solution molarity.

The diffusion overpotentials also derive from a simplified Butler–Volmer equation, if the reaction development is so favoured that the ratio (j/j_o) can be considered tending to zero (Eq. (20) and Eq. (21) for cathode and anode, respectively).

Since the hydroxide ion diffusion coefficient is higher than the oxygen and hydrogen ones, OH^- gradients can be neglected in both GDL and CL (the second in view also of its low thickness), usually avoiding stressful current densities above 2 A/cm^2. Water concentration ratios can also be simplified: at the anode a liquid solution is directly fed, while at the cathode water supply is guaranteed by good membrane properties working in a dry environment. Here, the diffusion overpotentials are only dependent on H_2 and O_2 (at the cathode and anode, respectively), which could not be removed as quickly as they are produced at increasing current densities and could partly block reaction sites by slowing down the kinetics. In theory, these polarisation losses are due to a concentration gradient formed between bulk (C^{bulk}) and electrode surface (C^{sur}). Surface concentrations locally vary by occurring reactions in the whole catalyst layer volume; however, a conservative approach consists of evaluating the gradient between the bulk and the concentration at the electrode-membrane interface (C^{memb}). Eq. (22) is finally obtained by solving Eq. (20) and Eq. (21) for ideal reversible electrodes, resulting in a Nernst-type formulation [24]. It is noteworthy that, according to the following assumptions, the reaction orders of hydrogen and oxygen are not evaluated for formulating exchange current densities since their bulk concentrations are considered almost constant. In other words, no previous constraint is imposed on equations of the diffusion overpotential. Otherwise, there would be a correlation between reaction orders used in the exchange current density and those used in the diffusion overpotential.

$$\eta_{diff} = \eta_{diff}^{cat} + \eta_{diff}^{an} = \frac{RT}{zF}\ln\left(\frac{C_{H_2}^{memb}}{C_{H_2}^{bulk}}\right)^{\gamma_1} + \frac{RT}{zF}\ln\left(\frac{C_{O_2}^{memb}}{C_{O_2}^{bulk}}\right)^{\beta_2} \tag{22}$$

Bulk concentrations are computed at the equilibrium conditions, while concentrations at the electrode-membrane interface are obtained by O_2 and H_2 simplified one-dimensional steady-state material balances solved along the electrode thickness. In the gas diffusion layer, Fickian diffusion is assumed to occur; in the catalyst layer, both diffusion and reaction occur. At the cathode, there is only the gas phase with ideal behaviour, working at atmospheric pressure. At the anode, the dissolved oxygen concentration has to be considered due to the presence of liquid electrolyte [8–28]. According to these hypotheses, Eq. (22) results in Eq. (23).

$$\eta_{diff} = \frac{RT}{zF}\ln\left[1 + \frac{jRT\left(\frac{d_c}{2} + \delta_c\right)}{zFD_{H_2,H_2O}^{eff}\left(p - p_{H_2O}^{sat}\right)}\right]^{\gamma_1} + \frac{RT}{zF}\ln\left[1 + \frac{\phi jH_{O_2,H_2O}\left(\frac{d_a}{2} + \delta_a\right)}{2zFD_{O_2,H_2O}^{eff}\left(p - p_{KOH}^{sat}\right)}\right]^{\beta_2} \tag{23}$$

$$\left(\frac{C_{H_2}^{sur}}{C_{H_2}^{bulk}}\right)^{\gamma_1}\left(\frac{C_{-(cat)}^{sur}}{C_{-(cat)}^{bulk}}\right)^{\gamma_2}\exp\left(\frac{\alpha_{cat}\ zF\eta_{diff}^{cat}}{RT}\right) - \left(\frac{C_{H_2O(cat)}^{sur}}{C_{H_2O(cat)}^{bulk}}\right)^{\beta}\exp\left[\frac{-(1-\alpha_{cat})zF\eta_{diff}^{cat}}{RT}\right] = 0 \tag{20}$$

$$\left(\frac{C_{-(an)}^{sur}}{C_{-(an)}^{bulk}}\right)^{\gamma}\exp\left(\frac{\alpha_{an}\ zF\eta_{diff}^{an}}{RT}\right) - \left(\frac{C_{H_2O(an)}^{sur}}{C_{H_2O(an)}^{bulk}}\right)^{\beta_1}\left(\frac{C_{O_2}^{sur}}{C_{O_2}^{bulk}}\right)^{\beta_2}\exp\left[\frac{-(1-\alpha_{an})zF\eta_{diff}^{an}}{RT}\right] = 0 \tag{21}$$

Where d and δ are the CL and GDL thickness at the anode or cathode, D_{H_2,H_2O}^{eff} the hydrogen effective diffusion coefficient in the cathodic gaseous mixture, H_{O_2,H_2O} the Henry's constant for oxygen, D_{O_2,H_2O}^{eff} the oxygen effective diffusion coefficient in the anodic liquid mixture, ϕ a

corrective factor to consider the fraction of the current density to produce the dissolved oxygen in the electrolyte. Refer to the Appendix section for the complete theoretical formulation of hydrogen and oxygen simplified material balances.

The hydrogen molecular diffusion coefficient ($D^{eff}_{H_2,H_2O}$ in [m^2/s]) derives from the Fuller law as a function of the temperature (T in [K]), the pressure (p in [atm]), the molecular weights (MM in [g/mol]) and the dimensionless diffusion volumes (V in [-]) [29]. This value is then corrected by the cathodic porosity (ε_{cat}) and tortuosity (τ_{cat}) (Eq. (24)). Note that equal values of porosity and tortuosity were assumed for the gas diffusion layer and the catalytic layer in a first approximation.

$$D^{eff}_{H_2,H_2O} = \frac{\varepsilon_{cat}}{\tau_{cat}}\left[\frac{1.43\cdot10^{-7}\ T^{1.75}}{p\left(\frac{2}{1/MM_{H_2}+1/MM_{H_2O}}\right)^{0.5}\left(V_{H_2}^{1/3}+V_{H_2O}^{1/3}\right)^2}\right] \quad (24)$$

In the anodic contribution, the Henry's constant (H_{O_2,H_2O} in [(atm·cm^3)/mol] is calculated by a literature empirical formulation as a function of temperature (T in [K]), referring to the oxygen dissolved in water in a range between 45 °C and 100 °C (Eq. (25)) [30].

$$H_{O_2,H_2O} = 5.08\cdot10^6\ \exp\left(\frac{-500}{T}\right) \quad (25)$$

The oxygen effective diffusion coefficient considers the gas bubble evolution (Eq. (26)), showing a semi-empirical dependence on the current density (j in [A/m^2]) [28]. The material transfer within gas-evolving electrodes depends on the produced oxygen bubble flow rate and the geometrical active area. Its validity limit recalls the points illustrated for Eq. (19) in view of the strong correlation between the bubble formation on the surface and the following transport within the solution.

$$D^{eff}_{O_2,H_2O} = k_{diff}(j)^{0.3}\frac{\varepsilon_{an}^{1.5}}{\tau_{an}}D_{O_2,\ H_2O} \quad (26)$$

Where ε_{an} and τ_{an} represent the porosity and tortuosity of the anode, respectively, which were assumed equal in GDL and CL in a first approximation, k_{diff} an empirical constant considering the bubble dual effect on the material transport. On the one hand, the bubble presence can enhance it by generating turbulence within the solution; on the other hand, it reduces the effective available diffusion path (i.e., decreasing electrode porosity). The oxygen molecular diffusion coefficient (D_{O_2,H_2O} in [cm^2/s]) is calculated using an empirical formulation as a function of temperature validated between 10 °C and 80 °C (T in [K]), as reported in Eq. (27) [31].

$$D_{O_2,H_2O} = 10^{\left[-4.410+\frac{773.8}{T}-\left(\frac{506.4}{T}\right)^2\right]} \quad (27)$$

2.1.3. Ohmic overpotential

Ohmic resistances are due to the electrical and ion resistances; nevertheless, the first ones are usually negligible with respect to contribution due to ion migration within the anodic alkaline solution, the membrane and the cathodic ionomer in a dry cathode configuration. This loss (η_{ohm}) is formulated by Ohm's law, assuming layers in series according to Fig. 1. Each resistance (ρ) is defined as the ratio between the material thickness (d) and conductivity (σ), adjusted by the effective volume fraction (ε) in the case of a non-continuous layer (Eq. (28)).

$$\eta_{ohm} = (\rho_{an}+\rho_{memb}+\rho_{cat})j = \left(\frac{d_{an}}{\sigma_{KOH}\varepsilon_{an}^{1.5}}+\frac{d_{memb}}{\sigma_{memb}}+\frac{d_{cat}}{\sigma_{ion}\varepsilon_{ion}^{1.5}}\right)j \quad (28)$$

Referring to the anode in detail, Eq. (28) considers the active electrode thickness (d_{an}), the KOH solution conductivity (σ_{KOH} in [S/cm]) expressed by an empirical correlation as a function of molarity (M in [mol/l]) and temperature (T in [K]) as shown in Eq. (29) [32], and the correct electrode porosity (ε_{an}) to consider the bubble presence too [8]. Eq. (29) has been validated for temperatures from 0 °C to 100 °C and KOH concentrations from 0 M to 12 M.

$$\sigma_{KOH} = -2.04\ M - 0.0027\ M^2 + 0.005332\ M\ T + 207.2\ \frac{M}{T} + 0.00105\ M^3 - 0.0000004\ M^2\ T^2 \quad (29)$$

For the membrane as well, the ohmic resistance (ρ_{memb}) is expressed as the ratio between its thickness (d_{memb}) and conductivity (σ_{memb}). Specifically, this last term results in the sum of the conductivities of available charge carriers (i.e., anions and cations), each multiplied by its transport number (λ), as shown in Eq. (30). The conductivity depends on their concentration within the membrane (C^{AEM}), their charge number (z) and their mobility (u), distinguishing the anions (defined as "-") and the cations (defined as "+").

$$\sigma_{memb} = \lambda_+\sigma_+ + \lambda_-\sigma_- = \lambda_+\left(z_+FC_+^{AEM}u_+\right) + \lambda_-\left(z_-FC_-^{AEM}u_-\right) \quad (30)$$

Since the cation mobility u_+ is lower than OH^- value [33], Eq. (30) can be rewritten as Eq. (31) (in other terms, λ_- equal to 1).

$$\sigma_{memb} = FC_-^{AEM}u_- \quad (31)$$

Working in dry conditions, the ion conduction at the cathode occurs across the ionomer, which usually has electrochemical properties very similar to those of the membrane. Therefore, in a first approximation, the cathodic resistance can be written as the ratio between the active electrode thickness (d_{cat}) and the ionomer conductivity (σ_{ion}), assumed equal to the membrane one and corrected by effective volumetric fraction (ε_{ion}) using Bruggeman's correlation [15].

According to previously discussed formulations, the polarization contribution due to the bubble evolution can be quantified and compared with an ideal system without penalising bubble effects. Indeed, each polarization loss includes a corrective coefficient: the activation overpotential by the bubble coverage factor that decreases the theoretical exchange current density, the ohmic overpotential by the porosity change in the anodic catalyst layer that decreases the conductivity with respect to a pure liquid solution, and the diffusion overpotential by the current density-dependent empirical parameter that influences the transport coefficient.

2.2. Experimental setup

The model was tuned on experimental data from a lab-scale cell. These tests were expressly performed to permit a preliminary validation of the developed code, since they were carried out in a limited range of the cell possible operation. Here, the applied working conditions and the cell structure were referred to common AEM electrolyser operation without any specific layout or performance optimisation. The sample consisted of a square-shaped cell. A commercial polimethylbenzimidazolium membrane was used with a KOH alkaline solution as the electrolyte. Both electrodes were made of a Ni-felt support, where Pt/C-based and Ni/Fe oxide-based electrocatalysts were applied to the cathode and the anode, respectively, via spray deposition. These electrode materials agree with AEM cell reference literature on lab-scale testing, which proposes platinum and metal oxides as catalysts for hydrogen and oxygen evolution reactions [34–36]. The experimental tests were performed at atmospheric pressure while the cell operated under dry cathode conditions (i.e., no liquid electrolyte was fed to the cathode) at a constant anodic flow rate of around 30 ml/min, varying the working temperature, applied current and fed anodic solution molarity (Table 1). Electrochemical Impedance Spectroscopy (EIS) analysis and polarisation

Table 1
Studied working conditions under electrolysis cell operation.

Temperature	Current density	KOH solution molarity
60–70 °C	0–2 A/cm^2	0.5–1 mol/l

Table 2
Kinetic parameter identification.

Kinetic parameter	Value	Reference
Activation overpotential		
Charge transfer coefficients	$\alpha_{cat} = 0.5$ $\alpha_{an} = 0.4$	[41] [42]
Pre-exponential coefficients in exchange current densities	$\tilde{k}^{*}_{cat} = 3.6\times10^{7}$ A/m^2 $\tilde{k}^{*}_{an} = 3.0\times10^{3}$ A/m^2	Experimental data fitting since correlated to electrode microstructure
OH^- kinetic orders in exchange current densities	$\gamma^{*}_{2} = 0$ $\gamma^{*} = 0$	EIS analysis
Activation energies in exchange current densities	$E^{cat}_{act} = 29.5$ kJ/mol $E^{an}_{act} = 43.6$ kJ/mol	[39] [40]
Ohmic overpotential		
Membrane and ionomer conductivity parameters	$\tilde{k}^{1}_{ohm} = 0.23$ S/cm^2 $\tilde{k}^{2}_{ohm} = 5.84$ (S l)/(mol cm^2)	EIS data fitting since correlated to material microstructure and cell assembling
Diffusion overpotential		
Oxygen diffusion parameter	$\phi/k_{diff} = 10^{-2}$ (A/m^2)$^{0.3}$	Experimental data fitting since correlated to electrode microstructure and assembling

curve measurements were performed using a BioLogic VMP-300 Potentiostat with a current booster.

3. Results and discussion

3.1. Experimental data and model tuning

The literature review has defined the theoretical background of the model, obtaining formulations that describe the physics of the AEM electrolysis cell. Specific parameters that consider working conditions and cell materials derived from previous research works or, if not available, from experimental results (Table 2). It is noteworthy that this has to be considered a preliminary tuning of the model; an additional, more detailed investigation could be performed focusing on the main physicochemical features of each cell layer.

Referring to EIS data, Fig. 2 reports the trends of ohmic and polarisation resistance as a function of temperature and fed solution molarity. The temperature dependence is minimal, also in view of the small possible working range to avoid membrane drying. Molarity shows a significant influence on the ohmic resistance with its drastic increase at molarity reduction due to a lower anodic conduction but, above all, the growth of the membrane resistance. Indeed, this last term can be influenced by the external environment due to different phenomena, such as osmotic deswelling and co-ion sorption [37]. Effects on the polarisation resistance are negligible, as already observed by [38] in the same molarity range.

Referring to the activation losses, since the experimental data show a minimum dependence on the electrolyte molarity, the reaction orders with respect to OH^- ions in exchange current densities (Eq. (17), Eq. (18)) were supposed to be equal to zero. While the activation energies in the Arrhenius-type formulation of the exchange current densities were derived from literature, resulting in 29.5 kJ/mol and 43.6 kJ/mol for Pt and transition metal-based electrodes, respectively [39,40] Only the pre-exponential coefficients ($\tilde{k}^{*}$) dependent on active site distribution and material microstructure were detected by experimental IV curve fitting since they are specific for each electrode. It is noteworthy that there is a higher value for the cathodic term since the hydrogen evolution reaction is favoured, resulting in a higher exchange current density (Table 2). Considering the charge transfer coefficients in the activation overpotential equations (Eq. (15), Eq. (16)), they were evaluated from Volcano plots. The hydrogen evolution reaction on a Pt-based electrocatalyst has an almost symmetric behaviour in reduction and oxidation processes, leading to a value of 0.5 [41] and permitting an explicit formulation of the cathodic activation overpotential as a function of the current density (Eq. (32)). In the case of the oxygen evolution reaction, the Ni-based catalyst results in a value of 0.4 [42].

$$\eta^{cat}_{act} = \frac{RT}{\alpha_{cat} zF}\,\mathrm{arcsinh}\left(\frac{j}{2j^{cat}_{0}}\right) \tag{32}$$

According to EIS analysis observations, the ohmic loss can be further simplified. Starting from Eq. (28) and assuming an equal formulation for membrane and ionomer conductivities (i.e., $\sigma_{memb} = \sigma_{ion}$), Eq. (33) is obtained where anion mobility is considered a constant in view of an almost temperature independent profile of the ohmic resistance derived from EIS analysis (Fig. 2). It is noteworthy that, as in the case of water activity in the Nernst equation (Eq. (5), Eq. (7)), a sufficiently high anion conductivity within the membrane is supposed to allow a basic environment also at the cathodic CL without feeding electrolyte solution in dry cathode cell operation.

$$\eta_{ohm} = \left[\frac{d_{an}}{\sigma_{KOH}\varepsilon^{1.5}_{an}} + \frac{\left(d_{memb} + \frac{d_{cat}}{\varepsilon^{1.5}_{ion}}\right)}{\sigma_{memb}}\right] j = \left[\frac{d_{an}}{\sigma_{KOH}\varepsilon^{1.5}_{an}} + \frac{\left(\frac{d_{memb}}{Fu_{-}} + \frac{d_{cat}}{Fu_{-}\varepsilon^{1.5}_{ion}}\right)}{C^{AEM}_{-}}\right] j \tag{33}$$

Eq. (33) can be rewritten considering C^{AEM}_{-} as a function of molarity,

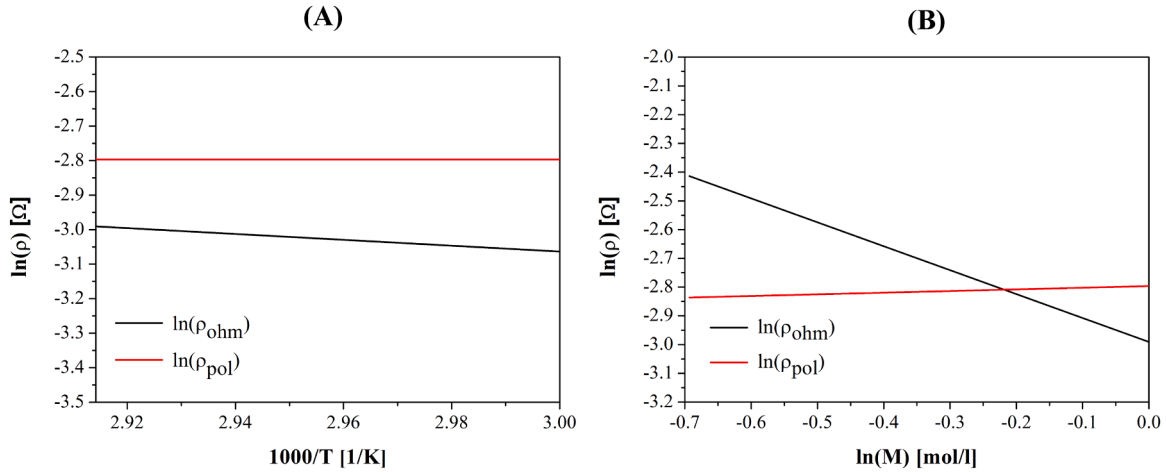

Fig. 2. Logarithmic plots of temperature (A) and molarity B) on ohmic and polarisation resistances derived from EIS analysis.

resulting in a more concise formulation for a model preliminary validation. Solving the Donnan equilibrium at the bulk solution-membrane interface [43–44], ion concentrations within the membrane depend on ion concentrations within the fed alkaline solution (i.e., solution molarity) (Eq. (34)). Simultaneously, OH^- concentration has to be equal to cation one, formulated as the sum of K^+ ion concentration and positive sites on the membrane, defined as Ion Exchange Capacity (IEC), to guarantee the electroneutrality in the membrane (Eq. (35)). Solving Eq. (34) and Eq. (35), a formulation for the OH- concentration is computed (Eq. (36)).

$$C_+^{AEM} C_-^{AEM} = K_D C_+^{bulk} C_-^{bulk} = K_D M^2 \tag{34}$$

$$C_-^{AEM} = C_+^{AEM} + IEC \tag{35}$$

$$C_-^{AEM} = \frac{IEC + \sqrt{IEC^2 + 4K_D M^2}}{2} \tag{36}$$

Where K_D is the Donnan equilibrium constant. Referring to the studied molarity range (Table 1), Eq. (36) can be rewritten in first approximation with a linear dependence on the solution molarity to obtain a simplified formulation of the ohmic polarisation (Eq. (37)).

$$\eta_{ohm} = \left(\frac{d_{an}}{\sigma_{KOH} \varepsilon_{an}^{1.5}} + \frac{1}{\tilde{k}_{ohm}^{1} + \tilde{k}_{ohm}^{2} M} \right) j \tag{37}$$

Where $\tilde{k}_{ohm}^{1}$ and $\tilde{k}_{ohm}^{2}$ are two empirical parameters that include microstructural features, such as thickness and ionomer volumetric fraction, as well as physicochemical features, such as ion mobility and ion exchange capacity of the membrane. Both were derived from EIS spectra fitting and are intended to be cell specific as including properties directly correlated to the cell materials and assembling.

Looking at diffusion losses (Eq. (23)), the anodic contribution (Eq. (38)) contains two unknown variables combinable into a unique empirical parameter (ϕ / k_{diff}) that was derived from IV curve fitting since it is also influenced by the electrode specific microstructure.

$$\eta_{diff}^{an} = \frac{RT}{2zF} \ln \left[1 + \frac{\phi j H_{O_2,H_2O} \left(\frac{d_a}{2} + \delta_a \right)}{2zFk_{diff} (j)^{0.3 \frac{\varepsilon_{an}^{1.5}}{\tau_{an}}} D_{O_2,\ H_2O} \left(p - p_{KOH}^{sat} \right)} \right]^{\beta_2} \tag{38}$$

Table 2 summarises applied kinetic parameters in this preliminary model validation. It is noteworthy that values correlated to the electrocatalyst intrinsic features, such as charge transfer coefficients, activation energies and reaction orders, are also applicable when testing other samples. Whereas extrinsic parameters linked to material microstructure, cell layer sintering and assembling could be variable, and for this reason they were specifically derived by experimental data fitting.

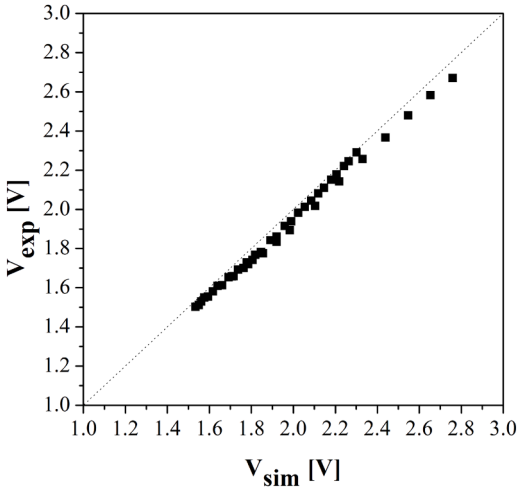

Fig. 3. Experimentally measured voltages vs. simulated voltages of AEM electrolyser.

Fig. 3 compares the measured and simulated cell voltage values, resulting in an average relative error of 2.5%.

3.2. Cell electrochemical characterization through modelling

Model tuning allowed for a preliminary characterization of the cell electrochemical performance, with the aim of distinguishing the contribution of different polarisation losses as well as the effects due to bubble evolution by evaluating the percentage weight of used corrective coefficients.

A sensitivity analysis was performed by varying the working temperature, the applied current density and the molarity of the fed anodic solution. The reference point consists of an operation at 60 °C, 1 M KOH and 1 A/cm^2. As already reported in [13,20] at this condition the main contribution is due to the activation overpotential, resulting in around 57% of the total losses, followed by the ohmic (around 32%) and the diffusion ones (around 11%). Applied load and electrolyte molarity have a significant influence on the cell performance, changing the weight of both activation and ohmic losses. Differently, the diffusion overpotential always results in the lowest term in each analysed case. In theory, the product accumulation in catalyst layers could slow down the electrochemical process. However, the hydrogen diffusion at the dry cathode has negligible effects in view of its small molecular size. The oxygen diffusion within the anodic solution is not the bounding factor as well, working far from the limiting current density.

Increasing temperature within a safety working range (Table 1) favours both the reaction development, the ion conduction and the reactant diffusion according to an Arrhenius-type dependence. Nevertheless, this variation has no visible effect on the weight of different cell losses on the total polarisation at a fixed electrolyte molarity (Fig. 4 A-B). While the current density increase causes a rise of all losses, resulting in higher percentages of the ohmic term in view of its linear dependence (Eq. (28)): around 6% vs. around 42% at 0.1 A/cm^2 and 2 A/cm^2, respectively, at each considered temperature. The activation overpotential remains the main contribution in view of the high ionic conductivity favoured by feeding 1 M KOH electrolyte. In the case of decreasing molarity (Fig. 4 C-D), there is a significant rise of the ohmic contribution correlated to ion conductivity worsening of both the alkaline solution (Eq. (29)) and the membrane that is influenced by the surrounding environment (Eq. (37)). While activation losses have no variation, considering the exchange current densities dependent just on temperature according to EIS analysis (Table 2). This leads to an increase of the ohmic loss percentage and a reduction of the activation one, above all at high currents where it becomes the main polarisation contribution (around 62% due to ohmic contribution vs. around 32% due to the activation term at 0.5 M KOH and 2 A/cm^2).

Multiple effects due to the bubble evolution were preliminarily investigated for each polarisation loss in view of their weight on the cell performance. Both anodic ohmic and activation losses are negatively influenced by the bubble presence, modifying the electrolyte conduction and the active site distribution. In the case of diffusion loss, there are two adverse phenomena. The bubble presence increases the transport path of the produced oxygen, slowing in theory the diffusion; on the other hand, their evolution can generate some turbulence that favours the material transport. Referring to the percentage weight of losses due to bubbles at variable temperatures (Fig. 5-A), there is no visible effect. While a significant increase is present at high current densities since more bubbles are generated in the system, reaching up to around 6.8% of the total losses at 2 A/cm^2. Variations on fed electrolyte molarity have a more evident influence (Fig. 5-B). Bubble growth depends on the current, but high molarity favours the ion conduction by reducing the weight of the bubble losses on the total polarisation: for instance, around 5% at 1 M KOH and 1 A/cm^2 vs. around 7% at 0.05 M KOH and 1 A/cm^2. The

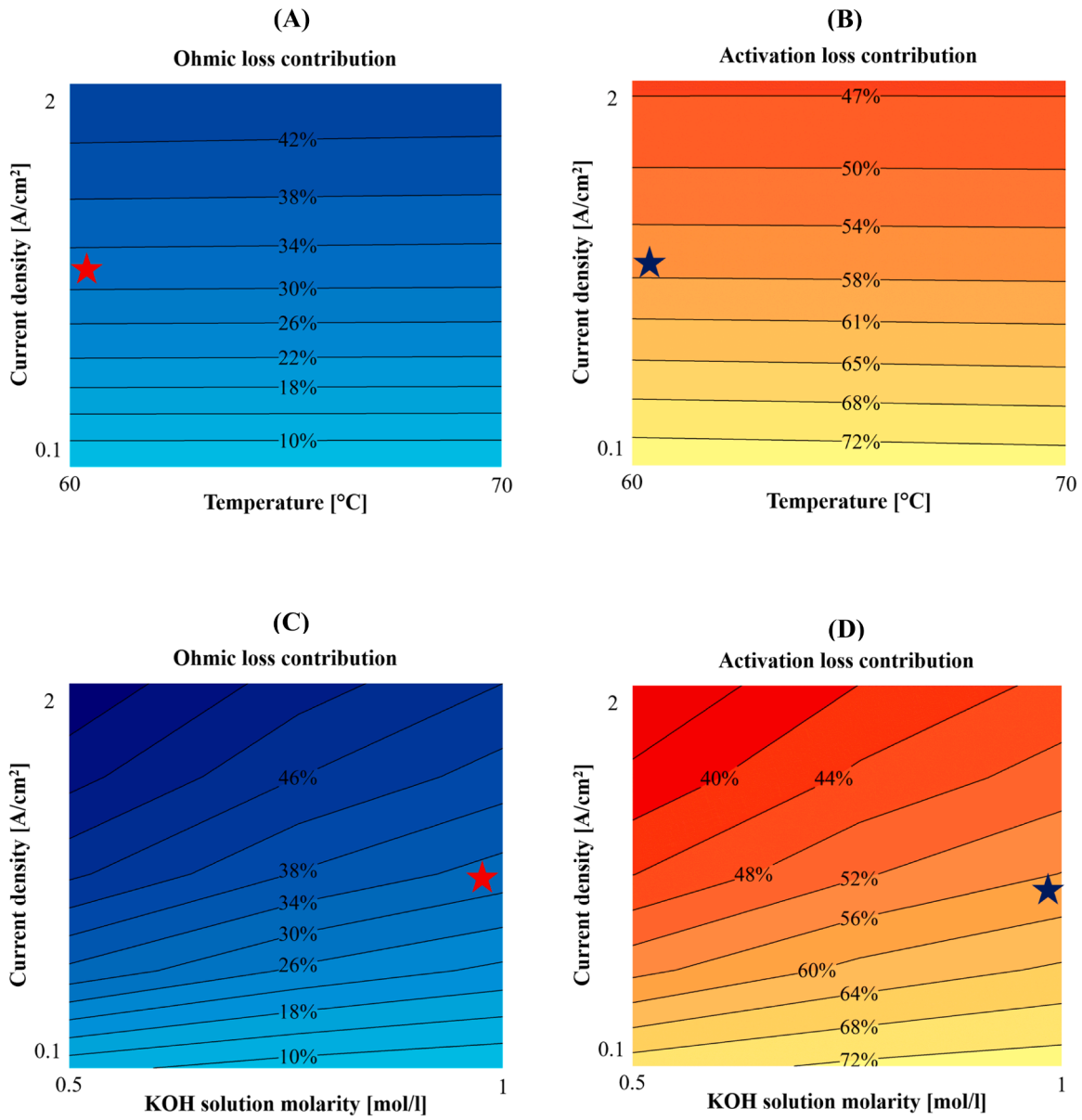

Fig. 4. Contribution of ohmic (A-C) and activation losses (B-D) with respect to total polarisation at variable temperatures and current densities (A-B), at variable electrolyte molarities and current densities (C-D); the stars point out the reference working point @60 °C, 1 M KOH and 1 A/cm^2.

maximum value of around 8.4% is reached at 0.05 M KOH and 2 A/cm^2.

Considering directly the influence on cell physicochemical properties allowed a more detailed investigation of occurring phenomena due to the bubble evolution. Bubble growth on the electrode surface penalises the electrochemical reaction, blocking the active sites and thereby reducing the exchange current density. According to the model, the effective active area decreases rapidly at low loads (around 82% at 0.1 A/cm^2), reaching then more gradually a value of around 55% at 2 A/cm^2, with the consequent halving of the exchange current density (Fig. 6-A). In view of these still high coverage factors, the anodic activation loss increases up to 2%. Bubble motion within the liquid reduces the ion conduction with respect to a monophase system by increasing the effective transport path. Here the anodic ohmic overpotential can reach up to 180 mV at 2 A/cm^2, with a direct influence on the cell total ohmic resistance, which increases around 15%. In other terms, the anodic solution shows an ion conduction characterising lower KOH concentrated liquids. For instance, at the reference working point of 60 °C and 1 MOH, the simulated conductivity of the alkaline electrolyte is reduced from 31 S/m without considering bubbles to 8 S/m considering bubbles, which would correspond to a solution at 0.02 M KOH and without bubbles. Finally, the oxygen transport is also influenced; at low currents the bubble presence penalises the transport by reducing the diffusion coefficient, while it improves at increasing currents since the positive effects due to turbulence prevail. Oxygen diffusion in water would be around 0.004 mm^2/s; this value decreases by around 20% under 0.05 A/cm^2 but then improves and doubles above 1 A/cm^2. Here a reduction of the diffusion losses is evaluated (Fig. 6-B). It is noteworthy that increasing currents would favour the diffusion referring to proposed formulations (Eq. (26)) compared to a system without bubbles; however, other factors should be balanced for values higher than 2 A/cm^2 working to the limiting current density.

4. Conclusions

Anion exchange membrane electrolysis cells are a promising technology for hydrogen generation, but further research studies are still needed to characterise the cell operation and optimise working conditions. Indeed, they are quite complex, resulting in a multi-phase system

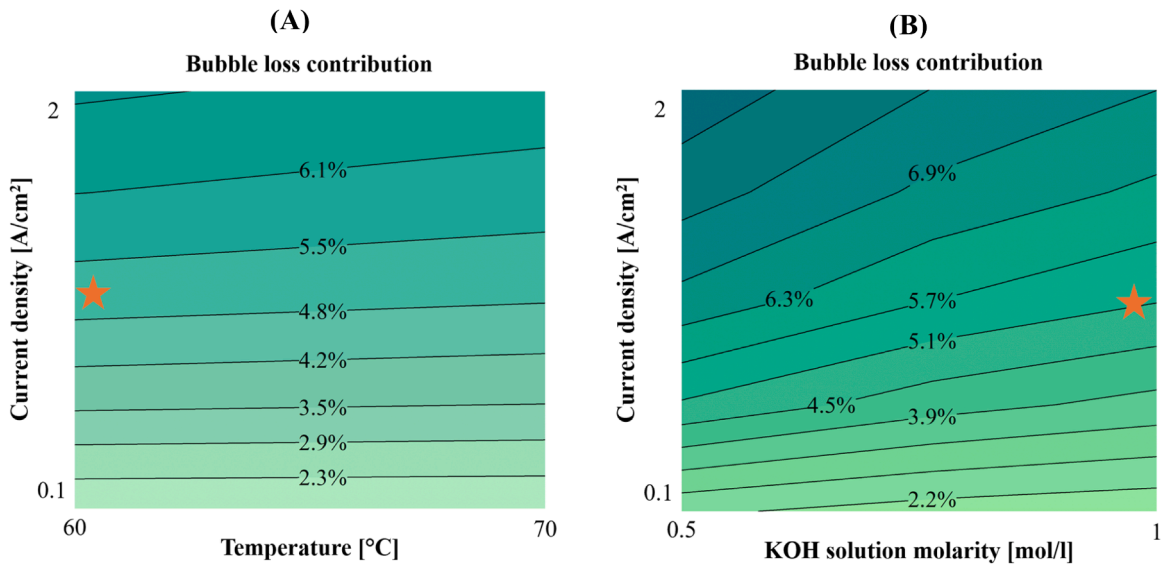

Fig. 5. Contribution of bubble losses with respect to total polarisation at variable temperatures and current densities (A), at variable electrolyte molarities and current densities (B); the stars point out the reference working point @60 °C, 1 M KOH and 1 A/cm^2.

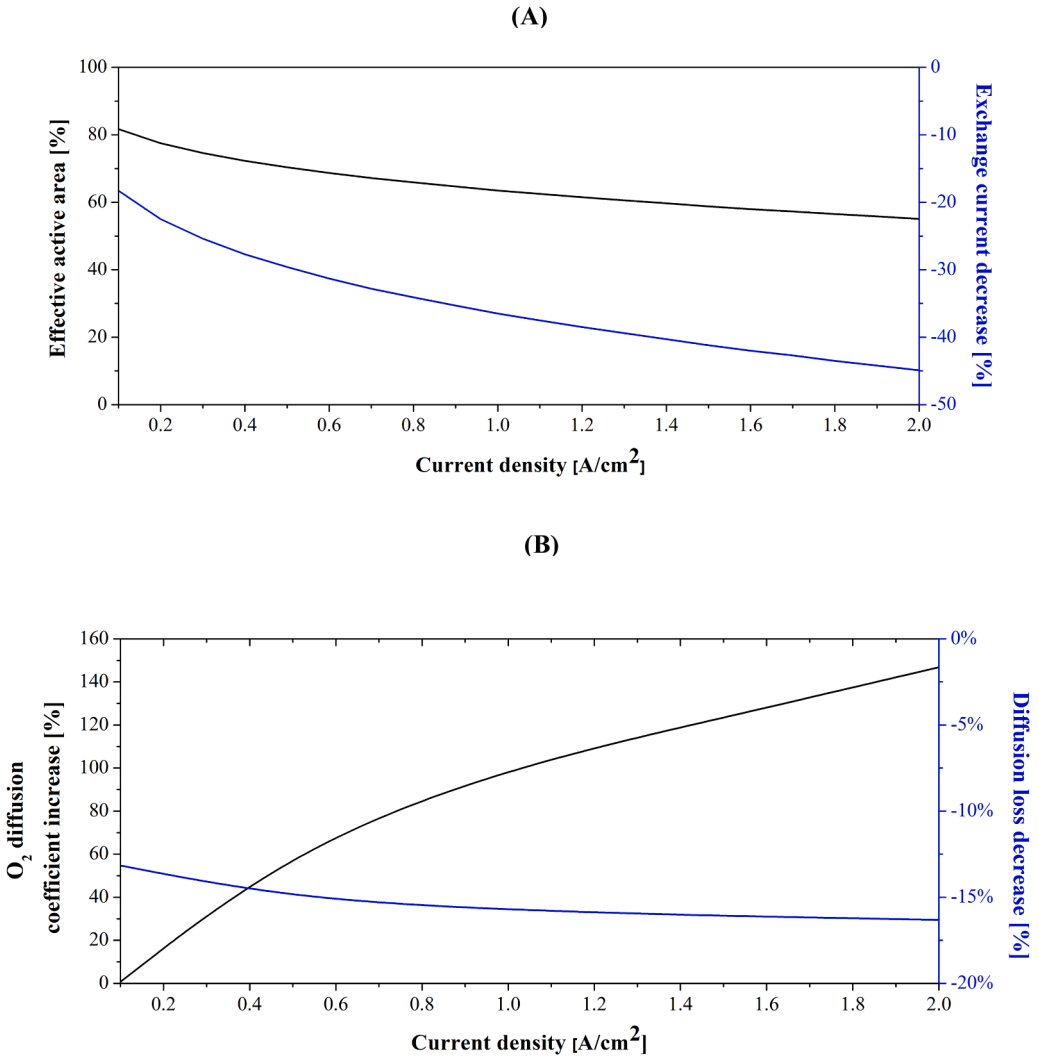

Fig. 6. Effects of bubble evolution on polarization losses referring to effective active area for the activation loss (A) and oxygen diffusion coefficient for the diffusion loss (B).

with asymmetric behaviour when the electrolyte is just fed at the anode side (i.e., dry cathode feed configuration). Starting from physically based principles, a theoretical formulation is presented to evaluate polarisation losses as a function of working and material parameters. Global cell performance in terms of voltage-current pair is correlated to local phenomena, such as ion migration within electrolyte and membrane, hydrogen and oxygen diffusion, bubble evolution in the alkaline solution. The result is a pseudo 0D model for anion exchange electrolysis cells, which was preliminarily validated by deriving some semi-empirical parameters on a lab-scale cell composed of state-of-the-art materials and tested in a limited range of temperatures and solution molarities. The developed simulation tool is suitable for performing a sensitivity analysis at variable current densities, working temperatures and fed anodic solution molarities. All polarisation losses depend on temperature, but the molarity value has the major influence on cell performance. The exchange current density seems independent from electrolyte molarity according to EIS analysis, while both anodic and membrane ohmic resistances significantly increase below 1 M KOH. The model evaluates the activation overpotential as the main contribution at high molarity values (reaching up to around 75% of the total losses at 0.1 A/cm^2, 1 M KOH and 60 °C), while the ohmic term prevails at lower molarity values (reaching up to 62% of the total losses at 2 A/cm^2, 0.5 M KOH and 60 °C). Bubble evolution at the anodic side leads to additional resistances that also represent around 8% of total losses. They are above all influenced by the applied current density, increasing the number of bubbles that block active sites and hinder species migration within the electrolyte. All these observations consist of preliminary results to be improved through following detailed material analysis and electrochemical testing that will allow a more rigorous model validation in wider ranges of working cases.

CRediT authorship contribution statement

Riccardo Venturino: Writing – review & editing, Visualization, Software, Methodology, Formal analysis. **Alessio D'Alessandro:** Writing – review & editing, Supervision, Methodology, Investigation, Conceptualization. **Laura Traversone:** Supervision, Project administration, Funding acquisition. **Fiammetta Rita Bianchi:** Writing – review & editing, Writing – original draft, Visualization, Software, Methodology, Conceptualization. **Barbara Bosio:** Writing – review & editing, Supervision, Project administration.

Declaration of competing interest

The authors declare that they have no known competing financial interests or personal relationships that could have appeared to influence the work reported in this paper.

Acknowledgements

This research was partially developed within the project "Turnkey electrochemical plants for H_2 production" - EU financed - Next Generation EU - PNRR-M2C2I5.2.

Appendix: details on activation and diffusion overpotential formulation

• Exchange current density formulation

The activation overpotential contribution, prevailing at low loads, is detected by assuming negligible concentration gradients between active sites and bulk, resulting in a simplified formulation of the Butler-Volmer equation (Eq. (15), Eq. (16)). In these formulas, the exchange current density represents the dynamic equilibrium condition, and it derives according to Eqs. A.1 and A.2, where reactant concentrations are only considered.

$$j_0^{cat} = zFk_{ox}^{cat}\left(C_{H_2}^{bulk}\right)^{\gamma_1}\left(C_{-(cat)}^{bulk}\right)^{\gamma_2}\exp\left[\frac{\alpha_{cat}zF\left(\Delta E_{rev}^{cat}-\Delta E_{rev}^{0}\right)}{RT}\right] = zFk_{red}^{cat}\left(C_{H_2O(cat)}^{bulk}\right)^{\beta}\exp\left[\frac{-(1-\alpha_{cat})zF\left(\Delta E_{rev}^{cat}-\Delta E_{rev}^{0}\right)}{RT}\right] \quad (A.1)$$

$$j_0^{an} = zFk_{ox}^{an}\left(C_{-(an)}^{bulk}\right)^{\gamma}\exp\left[\frac{\alpha_{an}zF\left(\Delta E_{rev}^{an}-\Delta E_{rev}^{0}\right)}{RT}\right] = zFk_{red}^{an}\left(C_{H_2O(an)}^{bulk}\right)^{\beta_1}\left(C_{O_2}^{bulk}\right)^{\beta_2}\exp\left[\frac{-(1-\alpha_{an})zF\left(\Delta E_{rev}^{an}-\Delta E_{rev}^{0}\right)}{RT}\right] \quad (A.2)$$

Solving the previous equations (Eqs. A.1 and A.2) and explicating the temperature dependence of the kinetic constants according to an Arrhenius-type law, Eq. A.3 and A.4 are obtained. Therefore, exchange current densities depend on both the reactant concentrations and the temperature.

$$j_0^{cat} = \widetilde{k}_{cat}\left(C_{H_2}^{bulk}\right)^{\gamma_1^*}\left(C_{-(cat)}^{bulk}\right)^{\gamma_2^*}\left(C_{H_2O(cat)}^{bulk}\right)^{\beta^*}\exp\left(\frac{-E_{act}^{cat}}{RT}\right) = \widetilde{k}_{cat}^{*}\left(C_{-(cat)}^{bulk}\right)^{\gamma_2^*}\exp\left(\frac{-E_{act}^{cat}}{RT}\right) \quad (A.3)$$

$$j_0^{an} = \widetilde{k}_{an}\left(C_{-(an)}^{bulk}\right)^{\gamma^*}\left(C_{H_2O(an)}^{bulk}\right)^{\beta_1^*}\left(C_{O_2}^{bulk}\right)^{\beta_2^*}\exp\left(\frac{-E_{act}^{an}}{RT}\right) = \widetilde{k}_{an}^{*}\left(C_{-(an)}^{bulk}\right)^{\gamma^*}\exp\left(\frac{-E_{act}^{an}}{RT}\right) \quad (A.4)$$

It is noteworthy that only the ion concentrations (C_{-}^{bulk}) are potentially relevant in Eq. (17) and Eq. (18). Indeed, bulk hydrogen, oxygen and cathodic steam concentrations derive from liquid/vapour equilibrium conditions, resulting in a function of the temperature with minimum variations between 50 °C and 75 °C. Moreover, anodic water composition is an almost constant value, feeding an excess solution.

• Bubble coverage factor formulation

At the anode (Eq. (16)), the effect of bubbles reducing the electrode surface is considered by the bubble coverage factor, which allows for calculating the effective active surface (A_{eff}) in Eq. A.5.

$$A_{eff} = A(1-\vartheta) \text{ with } \vartheta = \frac{N_{bubbles}\overline{A}_{bubble}}{A} \quad (A.5)$$

Where A represents the geometrical area, $N_{bubbles}$ the total number of bubbles and $\overline{A}_{bubble}$ the average area of a single bubble. The area of a single bubble is defined by assuming an ideal sphere of radius (r) that evolves during the time. Considering the bubble growth as the rate-determining step, the radius time change is expressed in Eq. A.6 and then substituted in the formula for the single bubble area (Eq. A.7).

$$r = b\sqrt{t} \text{ with } b = \frac{r_{max}}{\sqrt{t_r}} \tag{A.6}$$

$$A_{bubble} = \pi r^2 \sin^2(180^\circ - \varphi) = \pi \frac{r_{max}^2}{t_r} t \sin^2(180^\circ - \varphi) \tag{A.7}$$

Where b represents the kinetic constant defined as the ratio between the bubble radius just before detachment (r_{max}) and the square root of the bubble residence time (t_r), φ is the bubble contact angle.

With that aim of simplifying the previous formulation (Eq. A.7), an average area of a single bubble ($\overline{A}_{bubble}$) is introduced by the integral mean over the time (Eq. A.8).

$$\overline{A}_{bubble} = \frac{\int_0^{t_r} \pi \frac{r_{max}^2}{t_r} t \sin^2(180^\circ - \varphi) dt}{t_r} = \frac{\pi r_{max}^2 \sin^2(180^\circ - \varphi)}{2} \tag{A.8}$$

While the number of bubbles forming on the electrode ($N_{bubbles}$) is correlated to the gas volumetric flowrate $\left(f_{gas}\right)$, assuming again ideally spherical bubbles (Eq. A.9).

$$N_{bubbles} = \frac{f_{gas} 3 t_r}{4\pi r_{max}^3} \tag{A.9}$$

By combining Eq. A.8 and A.9, a formulation for the bubble coverage factor is obtained (Eq. A.10).

$$\vartheta = \frac{3 f_{gas} t_r \sin^2(180^\circ - \varphi)}{8 r_{max} A} \tag{A.10}$$

All terms in Eq. A.10 can be considered constants except for the gas flowrate, which depends on the applied current density through the Faraday law, resulting in the semi-empirical formulation of Eq. (19). It is noteworthy that a just fraction of the current density has to be considered since the produced oxygen both forms bubbles and dissolves within the solution.

- **Hydrogen and oxygen material balance formulation**

In the diffusion overpotentials (Eq. (23)), the concentrations at the electrode-membrane interface (C^{memb}) are computed by solving simplified one-dimensional steady state material balances in two control volumes (Fig. A1): one where only diffusion occurs (GDL - Gas Diffusion Layer) and one close to the membrane where both diffusion and reaction occur (CL - Catalyst Layer).

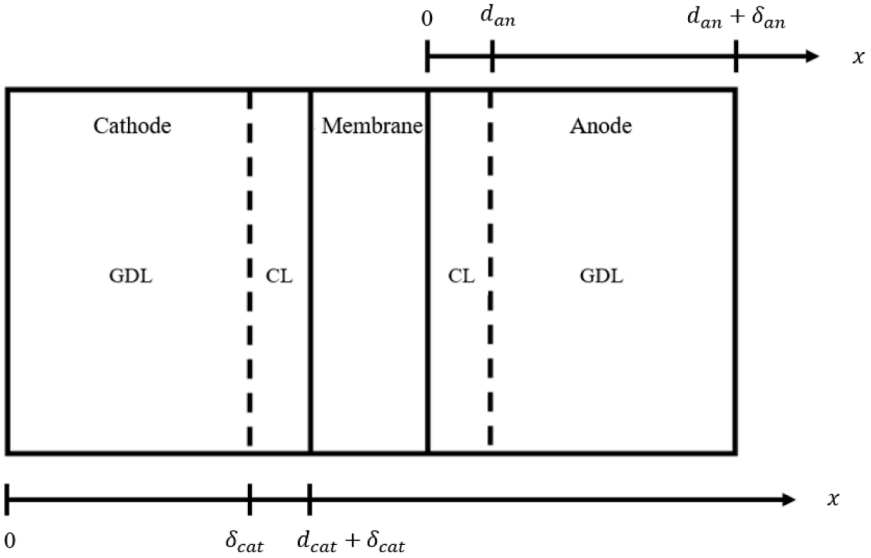

Fig. A1. Cell view specifying control volumes for cathodic and anodic 1D material balances (refer to bottom and top axes, respectively).

Under the assumptions of a steady-state, one-dimensional model and a Fickian diffusive flux, the hydrogen concentration profile in the cathodic GDL derives from the following material balance (Eq. A.11). As boundary conditions, L/V equilibrium according to Eq. (8) is considered for the bulk concentration (Eq. A.12), while the flux continuity is computed at the GDL-CL interface (Eq. A.13).

$$\frac{\partial^2 C_{H_2}}{\partial x^2} = 0 \tag{A.11}$$

$$x = 0 \rightarrow C_{H_2} = C_{H_2}^{bulk} = \frac{p - p_{H_2O}^{sat}}{RT} \tag{A.12}$$

$$x = \delta_{cat} \rightarrow D_{H_2,H_2O}^{eff} \frac{\partial C_{H_2}}{\partial x} = \frac{j}{zF} \tag{A.13}$$

Subsequently, the hydrogen concentration profile in the CL is computed by applying Faraday's law for the generation source (Eq. A.14). Boundary conditions derive the hydrogen concentration at the GDL-CL interface (Eq. A.15) from the previous balance in Eq. A.11 and consider a perfectly impermeable membrane to hydrogen flux at the CL-membrane interface (Eq. A.16).

$$-D^{eff}_{H_2,H_2O}\frac{\partial^2 C_{H_2}}{\partial x^2}=\frac{J^{cat}_{av}}{zF} \tag{A.14}$$

$$x=\delta_{cat}\rightarrow C_{H_2}=C^{bulk}_{H_2}+\frac{j\delta_{cat}}{zFD^{eff}_{H_2,H_2O}} \tag{A.15}$$

$$x=\delta_{cat}+d_{cat}\rightarrow\frac{\partial C_{H_2}}{\partial x}=0 \tag{A.16}$$

Where J_{av} is the average current for the unit of volume over the CL thickness.

Regarding the anodic compartment, the dissolved oxygen concentration has to be considered due to the presence of a liquid electrolyte [8,28]. In the anodic GDL, the material balance results in Eq. A.17 by assuming a Fickian diffusive flux. The boundary conditions assume L/V equilibrium according to Henry's law (Eq. A.18) and the flux continuity at the GDL-CL interface (Eq. A.19).

$$\frac{\partial^2 C_{O_2}}{\partial x^2}=0 \tag{A.17}$$

$$x=d_{an}+\delta_{an}\rightarrow C_{O_2}=C^{bulk}_{O_2}=\frac{p-p^{sat}_{KOH}}{H_{O_2,H_2O}} \tag{A.18}$$

$$x=d_{an}\rightarrow -D^{eff}_{O_2,H_2O}\frac{\partial C_{O_2}}{\partial x}=\frac{\phi j}{2zF} \tag{A.19}$$

The concentration profile in the CL is obtained by the following material balance (Eq. A.20), deriving from Eq. A.17 the oxygen concentration at the GDL-CL interface (Eq. A.21) and assuming an impermeable membrane to the oxygen flux at the CL-membrane interface (Eq. A.22).

$$-D^{eff}_{O_2,H_2O}\frac{\partial^2 C_{O_2}}{\partial x^2}=\frac{\phi J^{an}_{av}}{2zF} \tag{A.20}$$

$$x=d_{an}\rightarrow C_{O_2}=C^{bulk}_{O_2}+\frac{\phi j\delta_{an}}{2zFD^{eff}_{O_2,H_2O}} \tag{A.21}$$

$$x=0\rightarrow\frac{\partial C_{O_2}}{\partial x}=0 \tag{A.22}$$

It is noteworthy that the current density in Eq. A.14 and Eq. A.20 should be a function of both local reagent concentrations and potentials according to the Butler-Volmer equation when moving to one-dimensional modelling [45]. The formulation was here simplified, considering an average value by the integral of the current per the unit of volume mean over the CL thicknesses that results in a constant (Eqs. A.23 and A.24).

$$J^{cat}_{av}=\frac{\int_{x=\delta_{cat}}^{x=\delta_{cat}+d_{cat}}J(x)dx}{d_{cat}}=\frac{j}{d_{cat}} \tag{A.23}$$

$$J^{an}_{av}=\frac{\int_{x=0}^{x=d_{an}}J(x)dx}{d_{an}}=\frac{j}{d_{an}} \tag{A.24}$$

Solving previous material balances (Eqs. A.11, A.14, A.17 and A.20), the diffusion overpotentials result in Eq. (23).

Data availability

The data that has been used is confidential.

Reference

[1] H. Ishaq, I. Dincer, C. Crawford, A review on hydrogen production and utilization: challenges and opportunities, Int. J. Hydrog. Energy 47 (62) (2022) 26238–26264, https://doi.org/10.1016/j.ijhydene.2021.11.149.

[2] M. El-Shafie, Hydrogen production by water electrolysis technologies: a review, Results Eng. 20 (2023) 101426, https://doi.org/10.1016/j.rineng.2023.101426 no. July.

[3] F.R. Bianchi, B. Bosio, Operating principles, performance and technology readiness level of reversible solid oxide cells, Sustainability 13 (9) (2021), https://doi.org/10.3390/su13094777.

[4] S.J. Kim, J. Mahmood, P.W. Kang, Z. Xue, C.T. Yavuz, Challenges in electrolyzer performance evaluation for green hydrogen production, ACS Mater. Lett. 6 (7) (2024) 3168–3175, https://doi.org/10.1021/acsmaterialslett.4c00690.

[5] H.A. Miller, K. Bouzek, J. Hnat, S. Loos, C.I. Bernäcker, T. Weißgärber, L. Röntzsch, J. Meier-Haack, Green hydrogen from anion exchange membrane water electrolysis: a review of recent developments in critical materials and operating conditions, Sustain. Energy Fuels 4 (5) (2020) 2114–2133, https://doi.org/10.1039/c9se01240k.

[6] D. Henkensmeier, M. Najibah, C. Harms, J. Žitka, J. Hnát, K. Bouzek, Overview: State-of-the art commercial membranes for Anion exchange membrane water electrolysis, J. Electrochem. Energy Convers. Storage 18 (2) (2021), https://doi.org/10.1115/1.4047963.

[7] K. Lawand, S. Nuggehalli Sampathkumar, Z. Mury, J. Van Herle, Membrane electrode assembly simulation of anion exchange membrane water electrolysis, J. Power Sources 595 (2024) 234047, https://doi.org/10.1016/j.jpowsour.2023.234047 no. September 2023.

[8] X. Zhao, H. Ren, L. Luo, Gas bubbles in electrochemical Gas evolution reactions, Langmuir 35 (16) (2019) 5392–5408, https://doi.org/10.1021/acs.langmuir.9b00119.

[9] L.N. Stanislaw, M.R. Gerhardt, A.Z. Weber, Modeling electrolyte composition effects on anion-exchange-membrane water electrolyzer performance, ECS Meet. Abstr. 37 (2019), https://doi.org/10.1149/ma2019-02/37/1728 vol. MA2019-02, no1728–1728.

[10] L. An, T.S. Zhao, Z.H. Chai, P. Tan, L. Zeng, Mathematical modeling of an anion-exchange membrane water electrolyzer for hydrogen production, Int. J. Hydrog. Energy 39 (35) (2014) 19869–19876, https://doi.org/10.1016/j.ijhydene.2014.10.025.

[11] K. Jiao, S. Huo, M. Zu, D. Jiao, J. Chen, Q. Du, An analytical model for hydrogen alkaline anion exchange membrane fuel cell, Int. J. Hydrog. Energy 40 (8) (2015) 3300–3312, https://doi.org/10.1016/j.ijhydene.2014.12.091.

[12] D. Saebea, C. Chaiburi, S. Authayanun, Model based evaluation of alkaline anion exchange membrane fuel cells with water management, Chem. Eng. J. 374 (2019) 721–729, https://doi.org/10.1016/j.cej.2019.05.200, no. May.

[13] A.G. Vidales, N.C. Millan, C. Bock, Modeling of anion exchange membrane water electrolyzers: the influence of operating parameters, Chem. Eng. Res. Des. 194 (2023) 636–648, https://doi.org/10.1016/j.cherd.2023.05.004.
[14] E. Gul, G. Baldinelli, A. Farooqui, P. Bartocci, T. Shamim, AEM-electrolyzer based hydrogen integrated renewable energy system optimisation model for distributed communities, Energy Convers. Manag. 285 (2023) 117025, https://doi.org/10.1016/j.enconman.2023.117025 no. December 2022.
[15] E. Tardy, Y. Bultel, F. Druart, A. Bonnefont, M. Guillou, B. Latour, Three-dimensional modeling of Anion exchange membrane electrolysis: a two-phase flow approach, Energies 17 (13) (2024) 1–16, https://doi.org/10.3390/en17133238.
[16] D. Lee, M. Kim, J. Kim, I. Moon, J. Kim, Advanced CFD simulation of two-phase anion exchange membrane water electrolysis, Int. J. Hydrog. Energy 88 (2024) 322–332, https://doi.org/10.1016/j.ijhydene.2024.09.180, no. June.
[17] F.M. Nafchi, E. Afshari, E. Baniasadi, Anion exchange membrane water electrolysis: numerical modeling and electrochemical performance analysis, Int. J. Hydrog. Energy 52 (2024) 306–321, https://doi.org/10.1016/j.ijhydene.2023.05.173.
[18] R.K. Pandala, G. Serrela, F.F. Onanala, Y. Bultel, P. Schott, Performance evaluation of the Anion exchange membrane based Water electrolysis, in: 2022 10th International Conference on Systems and Control (ICSC 2022), 2022, pp. 102–107, https://doi.org/10.1109/ICSC57768.2022.9993826.
[19] G. De Dominici, B. Gabriel, Analytical study of over-voltages in alkaline electrolysis and their parametric dependencies through a multi-physical model, Int. J. Energy Res. 46 (3) (2022) 3295–3323, https://doi.org/10.1002/er.7382.
[20] J. Liu, Z. Kang, D. Li, M. Pak, S.M. Alia, C. Fujimoto, G. Bender, Y.S. Kim, A. Z. Weber, Elucidating the role of hydroxide electrolyte on anion-exchange-membrane water electrolyzer performance, J. Electrochem. Soc. 168 (5) (2021) 054522, https://doi.org/10.1149/1945-7111/ac0019.
[21] S. Obut, Mathematical modelling and performance analysis of an AEM electrolyzer, J. Sci. Rep.-A (2024) 27–39, https://doi.org/10.1016/j.cviu.2017.00.000, no.58.
[22] W.W. Yuan, K. Ou, S. Jung, Y.B. Kim, Analyzing and modeling of water transport phenomena in open-cathode polymer electrolyte membrane fuel cell, Appl. Sci. 11 (13) (2021), https://doi.org/10.3390/app11135964.
[23] L. Järvinen, P. Puranen, A. Kosonen, V. Ruuskanen, J. Ahola, P. Kauranen, M. Hehemann, Automized parametrization of PEM and alkaline water electrolyzer polarisation curves, Int. J. Hydrog. Energy 47 (75) (2022) 31985–32003, https://doi.org/10.1016/j.ijhydene.2022.07.085.
[24] A.J. Bard, L.R. Faulkner, Electrochemical Methods: Fundamentals and Applications, 2nd Ed, John Wiley & Sons Inc, 2001.
[25] F.R. Bianchi, B. Bosio, A. Baldinelli, L. Barelli, Optimization of a reference kinetic model for solid oxide fuel cells, Catalysts 10 (1) (Jan. 2020) 104, https://doi.org/10.3390/catal10010104.
[26] H. Vogt, R.J. Balzer, The bubble coverage of gas-evolving electrodes in stagnant electrolytes, Electrochim. Acta 50 (10) (2005) 2073–2079, https://doi.org/10.1016/j.electacta.2004.09.025.
[27] Y. He, Y. Cui, W. Shang, Z. Zhao, P. Tan, Insight into the bubble-induced overpotential towards high-rate charging of Zn-air batteries, Chem. Eng. J. 448 (2022), https://doi.org/10.1016/j.cej.2022.137782 no. April.
[28] H. Vogt, The concentration overpotential of gas evolving electrodes as a multiple problem of mass transfer, J. Electrochem. Soc. 137 (4) (1990) 1179–1184, https://doi.org/10.1149/1.2086624.
[29] B. Todd, J.B. Young, Corrigendum to 'thermodynamic and transport properties of gases for use in solid oxide fuel cell modelling' [J. Power Sources 110 (2002) 186–200] (S037877530200277X) (10.1016/S0378-7753(02)00277-X)), J. Power Sources 320 (2016) 349, https://doi.org/10.1016/j.jpowsour.2016.04.123.
[30] R.F. Mann, J.C. Amphlett, B.A. Peppley, C.P. Thurgood, Henry's Law and the solubilities of reactant gases in the modelling of PEM fuel cells, J. Power Sources 161 (2) (2006) 768–774, https://doi.org/10.1016/j.jpowsour.2006.05.054.
[31] P. Han, D.M. Bartels, Temperature dependence of oxygen diffusion in H_2O and D_2O," J, Phys. Chem. 100 (13) (1996) 5597–5602, https://doi.org/10.1021/jp952903y.
[32] R.J. Gilliam, J.W. Graydon, D.W. Kirk, S.J. Thorpe, A review of specific conductivities of potassium hydroxide solutions for various concentrations and temperatures, Int. J. Hydrog. Energy 32 (3) (2007) 359–364, https://doi.org/10.1016/j.ijhydene.2006.10.062.
[33] J.R. Varcoe, P. Atanassov, D.R. Dekel, A.M. Herring, M.A. Hickner, P.A. Kohl, A. R. Kucernak, W.E. Mustain, K. Nijmeijer, K. Scott, T. Xu, L. Zhuang, Anion-exchange membranes in electrochemical energy systems, Energy Environ. Sci. 7 (10) (2014) 3135–3191, https://doi.org/10.1039/c4ee01303d.
[34] N. Du, C. Roy, R. Peach, M. Turnbull, S. Thiele, C. Bock, Anion-exchange membrane water electrolyzers, Chem. Rev. 122 (13) (2022) 11830–11895, https://doi.org/10.1021/acs.chemrev.1c00854.
[35] I. Vincent, E.C. Lee, H.M. Kim, Highly active Ni–Fe based oxide oxygen evolution reaction electrocatalysts for Alkaline Anion exchange membrane electrolyser, Catalysts 12 (5) (2022), https://doi.org/10.3390/catal12050476.
[36] M. Yu, G. Moon, E. Bill, H. Tüysüz, Optimizing Ni-Fe oxide electrocatalysts for oxygen evolution reaction by using hard templating as a toolbox, ACS Appl. Energy Mater. 2 (2) (2019) 1199–1209, https://doi.org/10.1021/acsaem.8b01769.
[37] J.C. Díaz, J. Kamcev, Ionic conductivity of ion-exchange membranes: measurement techniques and salt concentration dependence, J. Memb. Sci. 618 (2021), https://doi.org/10.1016/j.memsci.2020.118718 no. August 2020.
[38] I. Vincent, E.C. Lee, H.M. Kim, Comprehensive impedance investigation of low-cost anion exchange membrane electrolysis for large-scale hydrogen production, Sci. Rep. 11 (1) (2021) 1–12, https://doi.org/10.1038/s41598-020-80683-6.
[39] W. Sheng, H.A. Gasteiger, Y. Shao-Horn, Hydrogen oxidation and evolution reaction kinetics on platinum: acid vs alkaline electrolytes, J. Electrochem. Soc. 157 (11) (2010) B1529, https://doi.org/10.1149/1.3483106.
[40] Z.Ž. Lazarević, Č. Jovalekić, A. Milutinović, D. Sekulić, V.N. Ivanovski, A. Rečnik, B. Cekić, N.Ž. Romčević, Nanodimensional spinel $NiFe_2O_4$ and $ZnFe_2O_4$ ferrites prepared by soft mechanochemical synthesis, J. Appl. Phys. 113 (18) (2013) 0–11, https://doi.org/10.1063/1.4801962.
[41] P. Quaino, F. Juarez, E. Santos, W. Schmickler, Volcano plots in hydrogen electrocatalysis-uses and abuses, Beilstein J. Nanotechnol. 5 (1) (2014) 846–854, https://doi.org/10.3762/bjnano.5.96.
[42] R. Xiang, L. Peng, Z. Wei, Tuning interfacial structures for better catalysis of water electrolysis, Chem. - A Eur. J. 25 (42) (2019) 9799–9815, https://doi.org/10.1002/chem.201901168.
[43] A.E. Kozmai, V.V. Nikonenko, S. Zyryanova, N.D. Pismenskaya, L. Dammak, L. Baklouti, Modelling of anion-exchange membrane transport properties with taking into account the change in exchange capacity and swelling when varying bathing solution concentration and pH, J. Memb. Sci. 590 (2019) 117291, https://doi.org/10.1016/j.memsci.2019.117291 no. May.
[44] A.H. Galama, J.W. Post, M.A. Cohen Stuart, P.M. Biesheuvel, Validity of the Boltzmann equation to describe Donnan equilibrium at the membrane-solution interface, J. Memb. Sci. 442 (2013) 131–139, https://doi.org/10.1016/j.memsci.2013.04.022.
[45] J.S. Newman, C.W. Tobias, Theoretical analysis of current distribution in porous electrodes, J. Electrochem. Soc. 109 (12) (1962) 1183, https://doi.org/10.1149/1.2425269.